Maneuski, D. et al. (2015) Edge pixel response studies of edgeless silicon sensor technology for pixellated imaging detectors. *Journal of Instrumentation*, 10, P03018

Version: Published

http://eprints.gla.ac.uk/102572/

Deposited on: 16 April 2015

Edge pixel response studies of edgeless silicon sensor technology for pixellated imaging detectors

Edge pixel response studies of edgeless silicon sensor technology for pixellated imaging detectors

D. Maneuski,[a,1] **R. Bates,**[a] **A. Blue,**[a] **C. Buttar,**[a] **K. Doonan,**[a] **L. Eklund,**[a]
E.N. Gimenez,[b] **D. Hynds,**[a] **S. Kachkanov,**[b] **J. Kalliopuska,**[c] **T. McMullen,**[a]
V. O'Shea,[a] **N. Tartoni,**[b] **R. Plackett,**[b] **S. Vahanen**[c] **and K. Wraight**[a]

[a]*SUPA School of Physics and Astronomy, University of Glasgow,*
G12 8QQ, United Kingdom

[b]*Diamond Light Source Ltd, Harwell Science and Innovation Campus,*
Didcot, OX1 10DE, United Kingdom

[c]*VTT Micro and Nanoelectronics,*
Espoo, FI-02044, Finland

E-mail: dima.maneuski@glasgow.ac.uk

ABSTRACT: Silicon sensor technologies with reduced dead area at the sensor's perimeter are under development at a number of institutes. Several fabrication methods for sensors which are sensitive close to the physical edge of the device are under investigation utilising techniques such as active-edges, passivated edges and current-terminating rings. Such technologies offer the goal of a seamlessly tiled detection surface with minimum dead space between the individual modules. In order to quantify the performance of different geometries and different bulk and implant types, characterisation of several sensors fabricated using active-edge technology were performed at the B16 beam line of the Diamond Light Source. The sensors were fabricated by VTT and bump-bonded to Timepix ROICs. They were 100 and 200 μm thick sensors, with the last pixel-to-edge distance of either 50 or 100 μm. The sensors were fabricated as either *n-on-n* or *n-on-p* type devices. Using 15 *keV* monochromatic X-rays with a beam spot of 2.5 μm, the performance at the outer edge and corners pixels of the sensors was evaluated at three bias voltages. The results indicate a significant change in the charge collection properties between the edge and 5th (up to 275 μm) from edge pixel for the 200 μm thick *n-on-n* sensor. The edge pixel performance of the 100 μm thick *n-on-p* sensors is affected only for the last two pixels (up to 110 μm) subject to biasing conditions. Imaging characteristics of all sensor types investigated are stable over time and the non-uniformities can be minimised by flat-field corrections. The results from the synchrotron tests combined with lab measurements are presented along with an explanation of the observed effects.

KEYWORDS: X-ray detectors; Hybrid detectors; Inspection with x-rays

---

[1]Corresponding author.

Contents

1 Introduction

The development of hybrid semiconductor pixel detectors is transforming the capabilities of synchrotrons, X-ray imaging in general and is used extensively in particle physics experiments. Amongst the features of hybrid pixel detectors are high contrast ratio, noise discrimination, high frame rate, room temperature operation and high spatial resolution. However, one of the major drawbacks for this technology is the inability to make large area imaging planes with zero dead space.

The hybrid pixel detector is a patterned semiconductor sensor (typically silicon) that has a pixellated Readout Integrated Curcuit (ROIC) connected to it via a series of small solder bumps. Each channel of the pixel sensor matches a readout channel in the chip. The individual readout chips are limited to the CMOS reticle size (roughly 25×25 mm^2 — depends on provider and process) while the sensors may be made large, with size limited by the diameter of the high resistivity silicon substrate (typically 6-inch). However, increasing sensor size lowers the yield of the device and dramatically increases cost. The perimeter of the sensor is normally surrounded by a guard-ring structure with a Current-Collection Ring (CCR) and a set of floating guard-rings to minimize the sensor's leakage current and prevent the current generated by the dicing saw damage flowing into the active region of the sensor. This perimeter of up to a few mm is a non-active area around the sensor, where deposited chargeis collected by the CCR instead of the pixels of the sensor.

Table 1. Characteristics of the devices used in the Diamond Light Source B16 test beam. Device names are given as follows. i.e. for J08-NP-100-50, J08 is a unique sensor number on a Timepix ROIC wafer, NP is senor type (n-type pixel implant on p-type bulk), 100 means sensor thickness and 50 refers to the last pixel-to-edge distance.

Device name	Pixel implant type	Bulk doping type	Bulk resistivity ($k\Omega \cdot cm$)	Sensor thickness (μm)	Last pixel-to-edge distance (μm)	Measured (calculated) depletion voltage (V)
F08-NN-200-50	n	n	5	200	50	24 (28)
C07-NP-100-100	n	p	10	100	100	9 (10)
J08-NP-100-50	n	p	10	100	50	9 (10)

Being able to remove the sensor's guard-ring structure allows sensors to be tiled close to each other, reducing dead spaces, therefore producing a continuous imaging field over a large area required by specific applications.

Several technologies have been developed to minimise the insensitive area around the sensor. An external guard can be implemented as a metal guard ring contacted to a highly doped implanted region surrounding the pixel array and separating it from the cut edges of the device and therefore the damage created by the dicing process [1, 2]. A technology has also been developed that uses Deep Reactive Ion Etching (DRIE) process to separate the individual sensors on the wafer and side implantation to form active-edges [3]. Another technology under development is scribe-cleave-passivate [4, 5]. This work reports on the results from characterisation of alternative active-edge fabrication process through DRIE and side implantation [6–8] to reduce the inactive edge of the silicon detector even further as detailed in the following sections.

2 Materials and methods

2.1 Active-edge fabrication technology and devices under test

The set of detectors under test was fabricated by VTT [9]. These included 100 and 200 μm thick sensors, with both 50 and 100 μm pixel-to-edge distance (defined as distance from the center of the pixel closet to the edge to the physical edge of the sensor) and on *n-on-n* and *n-on-p* types (*n*-type pixel implant on *n*- or *p*-type bulk). The critical fabrications steps are summarised as follows. The detector wafer is fusion bonded to a handling wafer and thinned down to the desired thickness. The 55×55 μm^2 pitch pixel structures to match the Timepix ROIC are produced using relevant photo-lithographic fabrication steps. DRIE is employed to form the physical edge of the sensor. This is followed by the ion implantation step to dope the sensor sidewalls. Finally the handle wafer is removed to release the individual detectors from the wafer. Further details on the technology and fabrication process can be found in [10]. This approach offers a reduction in distance between the physical edge and the first readable pixel to $20 - 50$ μm. All sensors were bump-bonded to Timepix ROICs. In this work three sensors were characterised electrically and using a micro-focus monochromatic X-ray beam at the Diamond Light Source synchrotron facility [11]. The summary of the device properties are shown in table 1.

2.2 Timepix ROIC and readout system

The Timepix ROIC [12] was employed to test the active-edge technology. The chip is a 256×256 matrix of 55×55 μm^2 pixels with a total active area of 14×14 mm^2. Each pixel of the chip has both analogue and digital components. The analogue part has a pre-amplifier, discriminator and threshold equalisation circuitry with leakage current compensation. The digital block is formed by the Timepix synchronisation logic and a 14-bit shift register/counter with overflow control and a local buffer.

The chip can operate in several modes including counting and time-over-threshold (ToT). In counting mode the counter is incremented each time the pre-amplifier output exceeds a given threshold. In ToT mode the counter clocks continuously while the signal pulse is above threshold, which gives a measure of the input X-ray energy. The chip periphery includes LVDS controls, an IO logic, a 256-bit fast shift register and digital-to-analog converters. The detector was connected to a PC via the dedicated readout interface FitPix [13]. The system allows full control of the chip and is capable of up to 80 frames per second readout speed. The Pixelman software [14] was used for data acquisition.

For all the measurements reported in this paper the devices were operated in counting mode. All pixels of the devices were equalised using noise edge. Subsequently, the discriminator level was set to just above the noise level, which was equivalent to the signal collected from a 5 *keV* X-ray photon.

2.3 Laboratory experimental setup

Electrical characterisation of the devices was performed at room temperature in a dark room laboratory environment. Bias voltage was supplied to the detectors through a *Keithey 237* high precision source measure unit and was controlled by Labview software. The voltage was ramped from 0 *V* until a value such that the current reached -1 μA. Each current reading was taken with a 1 *V* step and 1 second delay between readings. The measurement was repeated in reverse by ramping bias voltage back to 0 *V* under the same conditions. The results are presented in section 3.1.

The devices were uniformly illuminated with a X-ray tube to assess imaging capabilities. Each was positioned 50 *cm* from a mini X-ray generator capable of producing X-rays up to 50 *kVp* and 80 μA. A 1 *mm* diameter brass collimator was used with the system. For each measurement 100 images were acquired with 1 *s* exposure time to achieve approximately $8000 - 10000$ counts in each pixel. The final flat-field image was averaged and presented in section 3.2.

2.4 Diamond Light Source experimental setup

The beam scan experiments were performed at the *B*16 beamline of Diamond Light Source. The core part of the beamline is a double crystal monochromator which is capable of providing white or monochromatic beams with $2 - 20$ *keV* energy into the experimental hutch. The energy for this experiment using monochromatic focused beam was set to 15 *keV* with an attenuation length of 417 μm in silicon. This is well above the Timepix noise threshold of ~ 5 *keV*, yet low enough to achieve good detection efficiency in silicon.

A compound refractive lens (CRL) was employed to produce a micro-focused beam spot. A silicon *p-i-n* detector assisted the beam size measurement. The detector was positioned at the focal
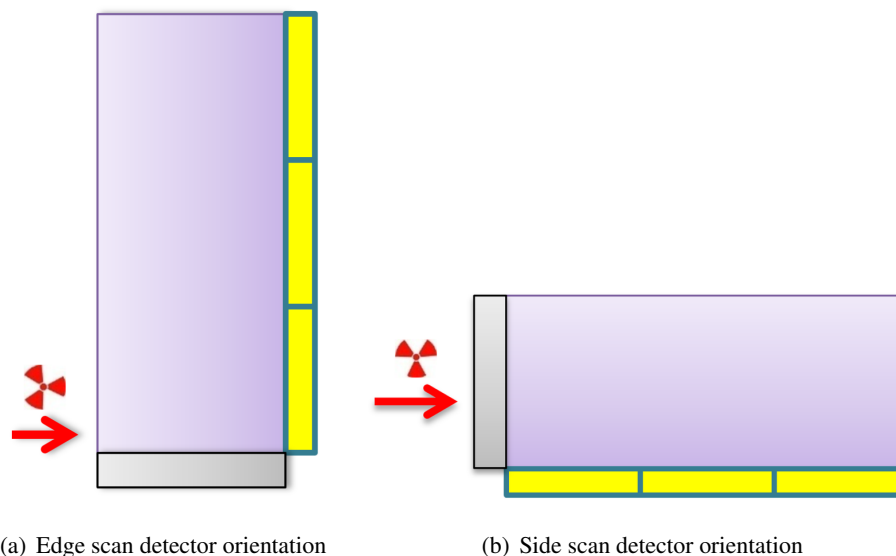
(a) Edge scan detector orientation   (b) Side scan detector orientation

Figure 1. Orientation of the detector with respect to the beam during experiments at Diamond Light Source B16 beamline. In the figures, yellow structure illustrates the pixel side of the sensor, while the grey shows the processed physical edge.

point of the CRL. The beam intensity was sampled in the X and Y directions with a 0.1 μm step and the derivative of the response of the silicon *p-i-n* detector was taken. The spot size at the detector focal plane was found to be 2.5 ± 0.1 μm FWHM in the X directions and 3.1 ± 0.1 μm FWHM in the Y direction. The comparatively small size of the beam profile allowed for sub-pixel resolution obtained from scans of various beam positions across adjacent pixels.

The modules were mounted in the hutch on a 6-axis precision translational and rotational stages to allow alignment and scanning. The device was positioned with the sensor's entrance window normal to the beam at the focal point of the CRL. The alignment of the device was achieved with the use of a visible wavelength laser. The laser was positioned to align with the beam and then shone at the sensor's surface. The device was moved until the laser spot was reflected back into the laser aperture. Using this method an angular alignment accuracy of 0.15 degrees was possible. The sensor was also aligned such that the pixel edges were parallel to the vertical and horizontal motor axes. This was achieved by moving the pixel array in the X-ray beam to illuminate pixels at extreme ends of a row (or column) of the device and the modules' response noted. The device was rotated until only one row (or column) of pixels was illuminated. This method gave a horizontal and vertical alignment of better than 0.2 degrees.

Several measurements were performed in this configuration. The first measurement was of energy resolution by means of a threshold scan with the Timepix ROIC operating in counting mode and the X-ray beam incident upon a pixel in the centre of the pixel array. All of the following measurements were performed with the Timepix working in counting mode and the threshold set to a value just above the noise floor, which is approximately 5 *keV*. For each beam position a number of frames with 100 *ms* integration time was recorded. The second measurement was the response of the device as the X-ray beam was scanned over the device's physical edge, called an *edge scan*

(see figure 1(a)). This was performed over the vertical edge at about the midpoint of the array. The X-ray was scanned from the centre of the $5th$ pixel from the edge to $25-125\ \mu m$ beyond the physical edge of the sensor in $2.5\ \mu m$ steps. The measurement was repeated for 3 different reverse bias voltages (30, 50 and 70 V) to understand the effect of over depleting the device (calculated depletion voltages can be found in table 1). The third measurement was similar to the second in that the X-ray beam was scanned over the corner of the sensor matrix to investigate the response of this region, called a *corner scan*. The scan started at the centre of the third pixel up and across from the corner pixel. The assembly was moved in 5 μm steps in a raster scan to cover the entire corner area of the device plus 25 μm beyond the physical edge in both the X and Y directions. This measurement was performed at a reverse bias of 50 V. The last set of measurements was a series of scans over the sides of the sensors, called a *side scan* (see figure 1(b)). The sensor was rotated by 90 degrees such that the edge of the sensor was normal to the direction of the beam. The intensity of the X-ray beam (15 keV) was sufficient to record X-ray hits from the beam for the full width of the pixel detector (14 $mm = 55\ \mu m \times 256$). To align the detector an image was recorded for a given rotation angle and motor position along axis. These were adjusted until the X-ray beam was contained within a given pixel row and crossed the entire matrix. Moving the matrix up and down and ensuring that the beam was contained within the matrix for the full height of the pixel array aligned for the rotation of the matrix around the beam direction. The sensor was reversed bias to 50 V. The assembly was scanned in the X-ray beam in 5 μm steps starting 50 μm before the array to 50 μm beyond the array and the response of the device recorded.

3 Results and discussion

3.1 Current-voltage characteristics

The devices were characterised for leakage current and breakdown before the synchrotron radiation tests as described in section 2.3. Figure 2 shows the response of each device until the current limited breakdown breakdown of $-1\ \mu A$ is reached. Sensor breakdown occurs well above the calculated depletion voltages. Device C07-NP-100-100 with a depletion voltage of $-10\ V$ breaks down at approximately $-80\ V$. Sensors F08-NN-200-50 and J08-NP-100-50 have different thicknesses, but both break down at approximately $-65\ V$. Both devices show similar breakdown voltages of $-65\ V$, which suggest this is a function of the last pixel to edge distance, and therefore the voltage at which electric field lines reach the physical edges of the device. The leakage current of all devices remained stable over the period of measurements. However, some hysteresis in leakage current is observed. This could be attributed to the excessive amount of certain defects in the edges of the sensor.

3.2 Flat-field measurements with X-ray tube

Devices under test were characterised for the purpose of imaging using X-rays at various tube peak voltages. Negligible differences in response were observed. Figure 3 shows flat-field images taken with an X-ray tube set to 50 kVp and 80 μA. Devices J08-NP-100-50 and C07-NP-100-100 demonstrate fairly uniform response with an occasional noisy pixel scattered randomly across the matrix. These pixels remain stable in time and space indicating their fixed nature and therefore can be corrected for imaging applications. In contrast, detector F08-NN-200-50 shows a very non-uniform
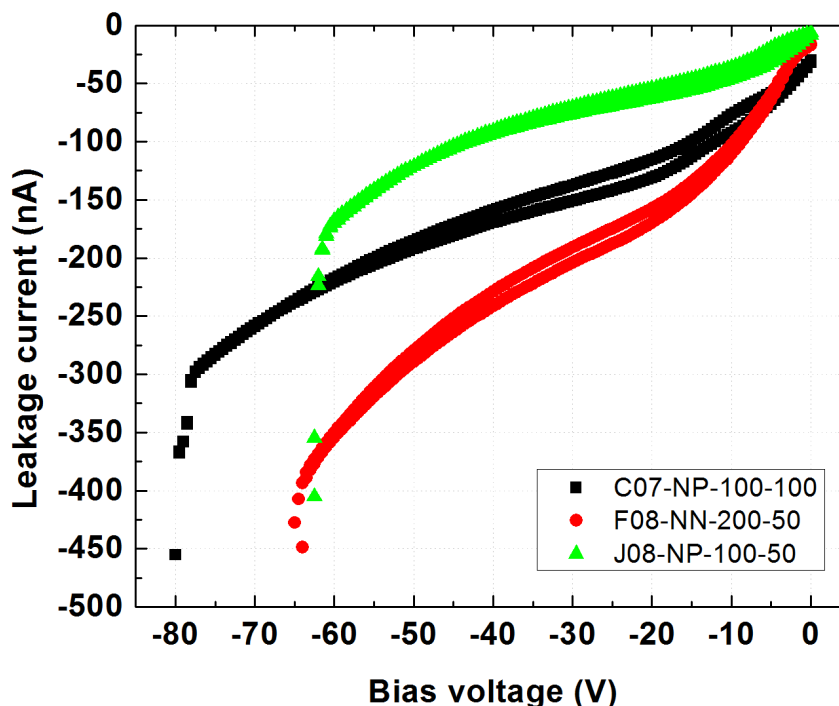
Figure 2. Current-voltage characteristics of the devices tested at Diamond Light Source. The bias voltage was gradually ramped up with 1 V/s and returned to 0 *V* with current recorded at each bias voltage.

response to the X-ray illumination, as shown in figure 3(a). The non-uniformities are possibly related to the handling wafer removal process. It is seen on the *n-on-n* wafers because of the rectifying junction is on the side bonded to the handle wafer and more susceptible to damage from the bonding/unbonding of the handle wafer. Further stability tests demonstrated that the pattern remains very stable in time and can be minimised by a flat-field correction for imaging purposes. Figure 3(d) quantifies the uniformity of all three devices by showing the normalised horizontal (or X-axis) projection, where normalised counts were calculated as counts in the pixel projection divided by median of the projected pixels. If three edge pixels at each side are excluded from calculations the standard deviation divided by mean value indicates relative matrix non-uniformity. This was found to be 5% for F08-NN-200-50, less than 1% for C07-NP-100-100 and J08-NP-100-50. The F08-NN-200-50 sensor shows 4 high count pixels at the perimeter compared to 2 pixels for the C07-NP-100-100 and J08-NP-100-50 sensors. It should be also noted that the first pixel from the edge for the F08-NN-200-50 sensor counts approximately 30% of the average. These effects were later studied in detail with micro-focused monochromatic X-ray beam as detailed in sections 3.4–3.5.

3.3 Energy resolution performance

The monochromatic X-ray beam was focused on a pixel near the centre of the matrix of the F08-NN-200-50 device. A series of measurements were made by increasing Timepix discriminator threshold values for an acquisition time of 100 *ms* per discriminator value. The number of counts in a 3 × 3 array centred on the pixel of X-ray incidence was plotted as a function of the threshold
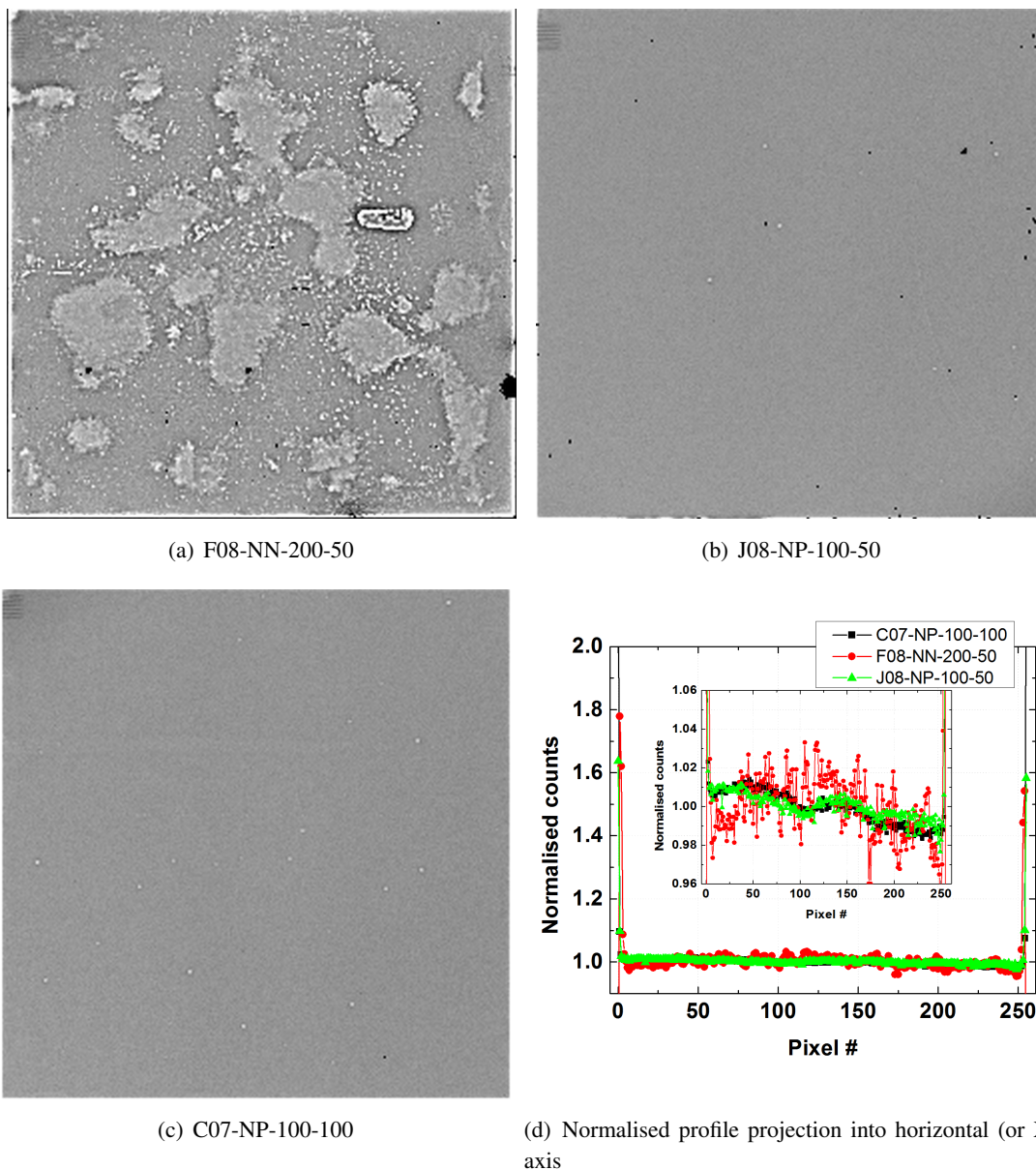
(a) F08-NN-200-50

(b) J08-NP-100-50

(c) C07-NP-100-100

(d) Normalised profile projection into horizontal (or X) axis

Figure 3. Flat-field images from the active-edge devices. X-ray tube was operated at 50 kVp and 80 μA current, devices were biased at $-50\ V$. Figure (d) illustrates projection of the flat-field images into the horizontal (or X) axis.

setting (see figure 4). An FFT filter was applied to the data set to smooth out statistical errors and a derivative was taken, resulting in a Gaussian peak. The centre of the peak corresponds to the energy of the X-ray beam of 15 keV and the width to the energy resolution of the device. Assuming the noise floor is $\sim 5\ keV$, an ADC conversion gave an energy resolution of 2 keV FWHM, which is typical for silicon Timepix sensors [15].
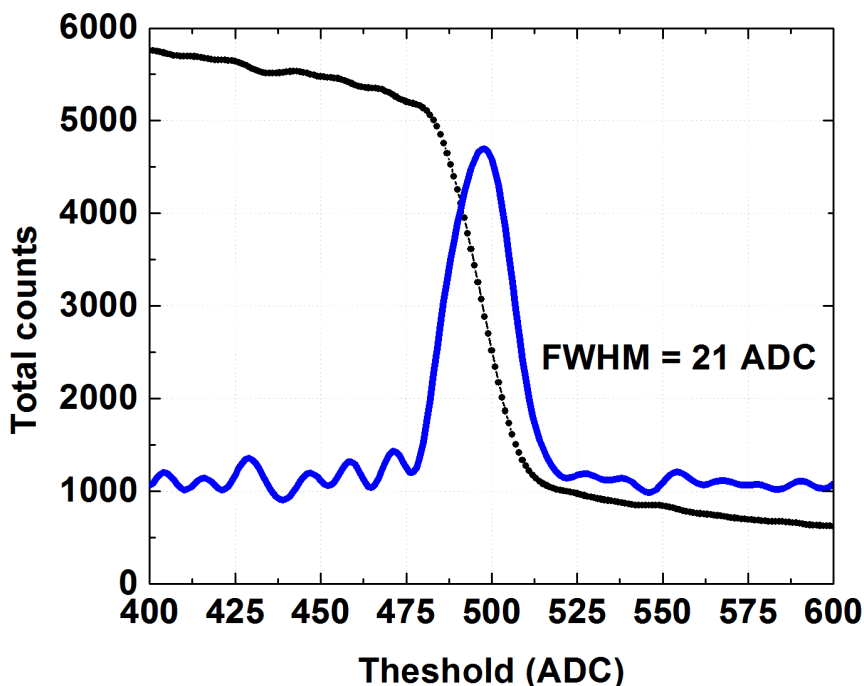
Figure 4. Threshold scan of the F08-NN-200-50 with a 15 *keV* X-ray beam illuminated in the centre of a pixel in the middle of the detector. The energy resolution is estimated to be 2 *keV* FWHM, which is typical for an ordinary device with silicon sensor coupled to Timepix ROICs.

3.4 Synchrotron edge scans

The response of each pixel at each beam position is shown in figure 5. In each plot the individual pixel responses are shown. The sum of each pixel response is also overlaid on top. The expected standard pixel response, seen in the case of the pixels farthest from the edge of each detector, have a plateau of charge collection around the centre of the pixel with falling edges as the beam approaches the pixel edges. The gradient of the measured profile for the pixels farthest from the edge is attributed to the charge sharing effects and the size of the beam spot. As the pixel thresholds ($E_{thr} = 5$ *keV*) were set lower than half of the incident X-ray energy ($E_{xray/2} = 7.5$ *keV*) double counting is observed when the beam is close to the pixel boundaries. The centres and dimensions of the farthest from the edge pixels are evident from the charge collection profiles. The physical edge of the detector is deduced by extrapolating the pixels pitch (55 μm) and known last pixel-to-edge distance (see table 1).

In the case of F08-NN-200-50 (see figure 5(a)), the influence of the edge implantation can be observed over the three outermost pixels. As the beam position crosses the physical edge of the detector, charge is collected in the two outermost pixels. The third starts to collect charges when X-ray beam is moved to 50μm away from the edge. The charge is predominantly collected in pixel 2. Charge collection in the outermost region is heavily distorted, with charge deposited in the edge region directed as far as 3 pixels from the interaction point (up to 110 μm away from the point of deposition). This indicates the significant non-uniformity of the electrical field in the edge region for this n-on-n device.
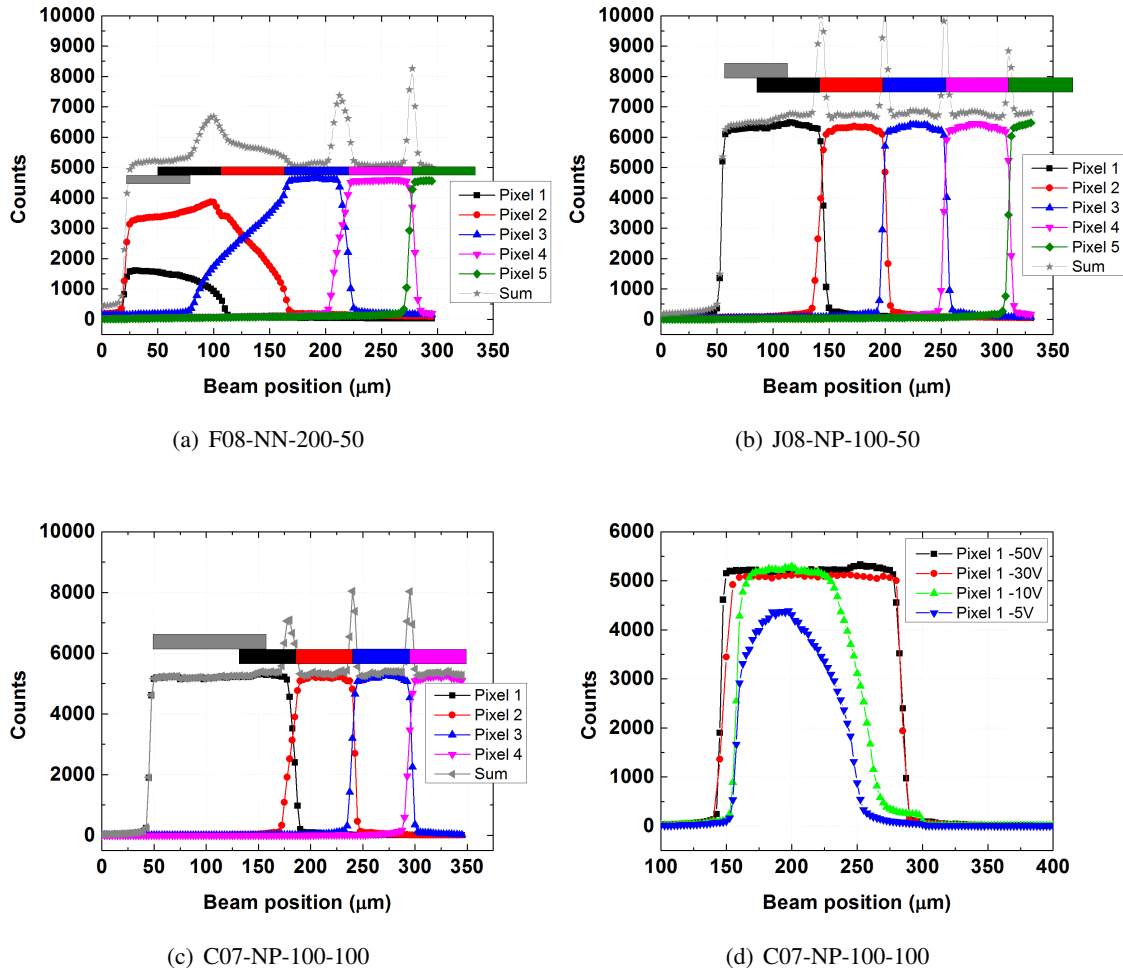
Figure 5. (a) - (c) Edge pixel responses as a function of incident beam position for a reverse bias of 50 *V*. The beam is normally incident on the detector. Colour rectangles represent physical pixels of 55 *µm* pitch and the distance of the first pixel to the physical edge of the device. (d) shows the effect of bias voltage variation on C07-NP-100-100.

In the case of J08-NP-100-50 (see figure 5(b)), little distortion of the charge collection is observed, even on the outermost pixel. There is good agreement in the charge collection behaviour over all the pixels. In addition, the active region of the outermost pixel extends to the physical edge of the detector without a significant loss in pixel response in the 25 *µm* beyond the dimension of the pixel. This indicates that the charge generated in the first 50 *µm* from the edge is not lost, but collected by the pixel closest to the edge. The summed charge distribution shows smaller regions of double counting (∼ 20 um) compared to the F08-NN-200-50 case of > 30 *µm*, which is attributed to the difference in sensor thickness. The effective width of the first pixel from the edge is 92 *µm*. The second outermost pixel (pixel 2) appears 60 *µm* wide, which is 3 % increase compared to 58 *µm* for pixel 3 and pixel 4. These were calculated as the distance between pixel edges at half hight of the response.

In the case of C07-NP-100-100 (see figure 5(c)), there is no evidence of large inter-pixel overlap regions as seen in the measurement on F08-NN-200-50. In fact the synergy of response behaviour between C07-NP-100-100 and J08-NP-100-50 is seen in the summed distribution where the regions of double counting are of similar extent. Effective width of the outermost pixel (pixel 1) is 140 μm, while pixel 2 and 3 are consistent with J08-NP-100-50 being 60 μm and 58 μm respectively. Figure 5(d) shows the effect of bias voltage on charge collection of pixel 1 for C07-NP-100-100. The results indicate that in order to collect all charges in the region close to the edge, a bias voltage of at least 20 V above the depletion voltage is needed. It is concluded that in the case of F08-NN-200-50 the increase in charge sharing in the outer pixels indicates the severe distortion of electrical field lines inside the device. This is consistent with having a thicker bulk device which is depleted from the opposite side relative to the other devices [1]. In general, these edge scans show that sidewall implantation was successful in achieving a fully active pixel sensor. Minimal charge collection distortion is achieved in the case of thin sensors. The results from 200 μm thick *n-on-n* sensor showed extreme field distortions and charge collection redistribution between the pixels.

3.5 Synchrotron corner maps

In this measurement the sensor was normal to the incident radiation as in the case of the edge scans. The X-ray beam was scanned over the detector along *horizontal* and *vertical* directions in 5 μm steps creating a 2-dimensional sub-pixellated map of charge collection. In each case the beam position exceeded the physical limit of the detector on each side of a corner region to show the effect on pixel response.

The response maps for each of the three devices are shown in figure 6. The most intense charge collection areas are the inter-pixel regions where double counting occurs, such that the pixel collects not only the charge when the beam position is within its own boundary but also when the beam is incident within its neighbour's boundary. This gives approximate pixel dimensions on the map as well as effective pixel sizes (effective area of charge collection for the pixel).

In the case of F08-NN-200-50 (see figure 6(a)) the map shows four pixels at the corner of the sensor, with the physical edges to the left and bottom of the plot. If the high charge collection regions are taken as approximately following the inter-pixel boundaries it is clear that there is some distortion of the boundaries which are ideally expected to be parallel to the detector edges. Further, the edge pixels, especially the bottom left, collect charge in regions exceeding the dimension of a single pixel of 55 μm × 55 μm. It suggests that the doping profiles and the associated techniques used in the fabrication of the *n-on-n* sensors are not as well defined as those used for the *n-on-p* sensors.

For J08-NP-100-50 (see figure 6(b)), the maps covers a region crossing nine pixels at the corner of the sensor, with the physical edges to the left and bottom of the plot. The high charge collection regions are more parallel than F08-NN-200-50, which is supposed to be the characteristic behaviour of an ideal sensor. On the side where the physical edge is visible the edge pixels have sensitive areas extending to the physical edge closer than > 55 μm from the cut edge.

In the case of C07-NP-100-100 (see figure 6(c) and 6(d)), the maps show regions crossing nine pixels at the corner of the sensor, with the physical boundaries to the bottom and to the left of the plot for figure 6(c) and to top and right for figure 6(d). Again, as in the J08-NP-100-50 case,
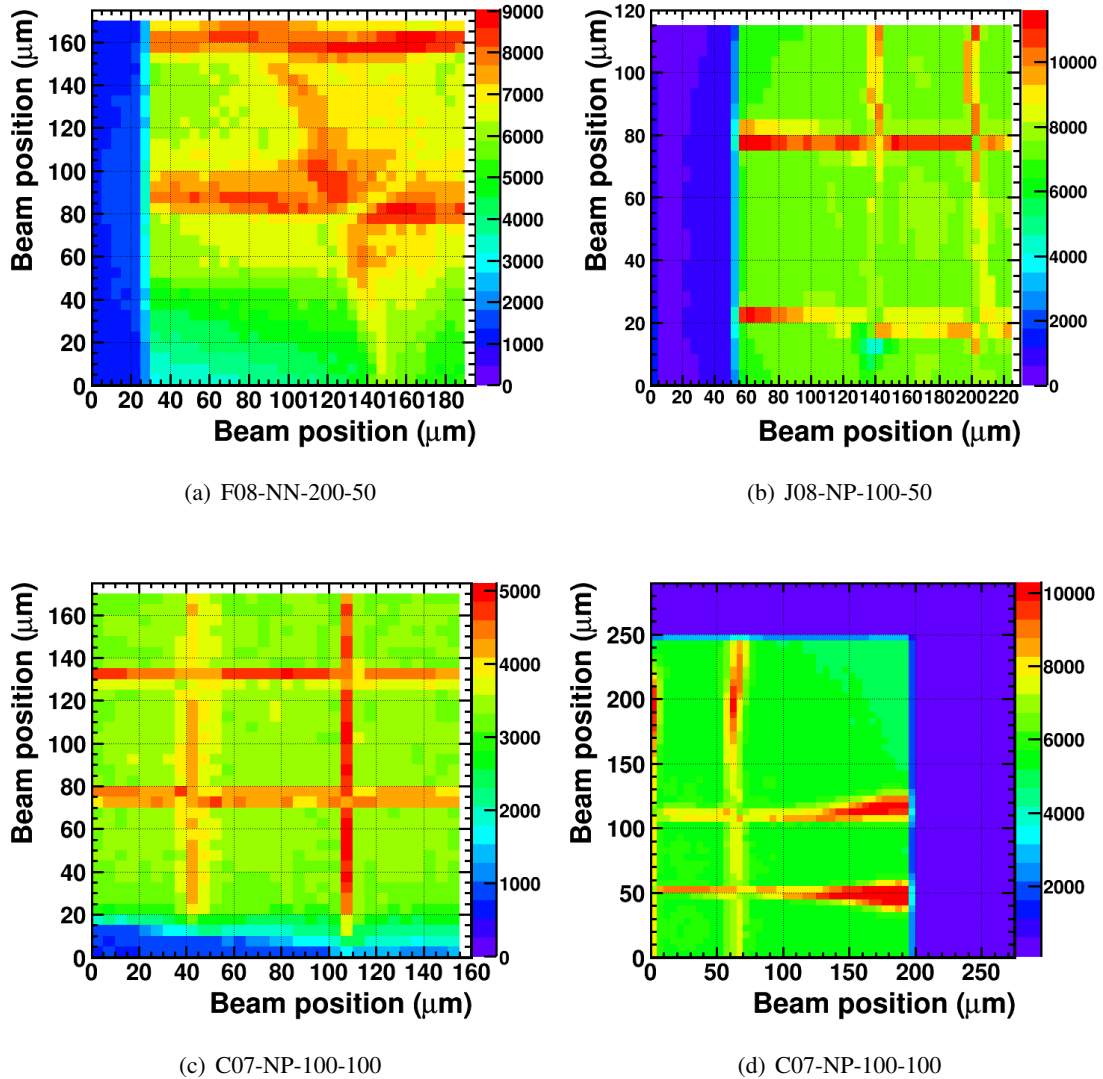
(a) F08-NN-200-50

(b) J08-NP-100-50

(c) C07-NP-100-100

(d) C07-NP-100-100

Figure 6. Corner maps scanned with 5 μm step as a function of position of incident synchrotron X-ray beam for a reverse bias of 50 V. Beam is normally incident on the detector.

the high charge collection regions behave like an ideal sensor, and the pixels next to the visible boundary collect charge beyond the 55 μm pixel size. Further as the beam position moved across the lower edge pixels towards the left side of the sensor edge (figure 6(c)), the sensitive region of the pixels in Y-direction decreases from ~ 75 μm for the bottom right pixel to ~ 60 μm for the bottom left pixel. This behaviour is explained by the distortion of the electric field inside the corner pixels of the sensor. This would not be seen for the F08-NN-200-50 and J08-NP-100-50 cases as the pixel-to-edge distance is smaller and the electric field could still influence charge collection up to the detector edge.
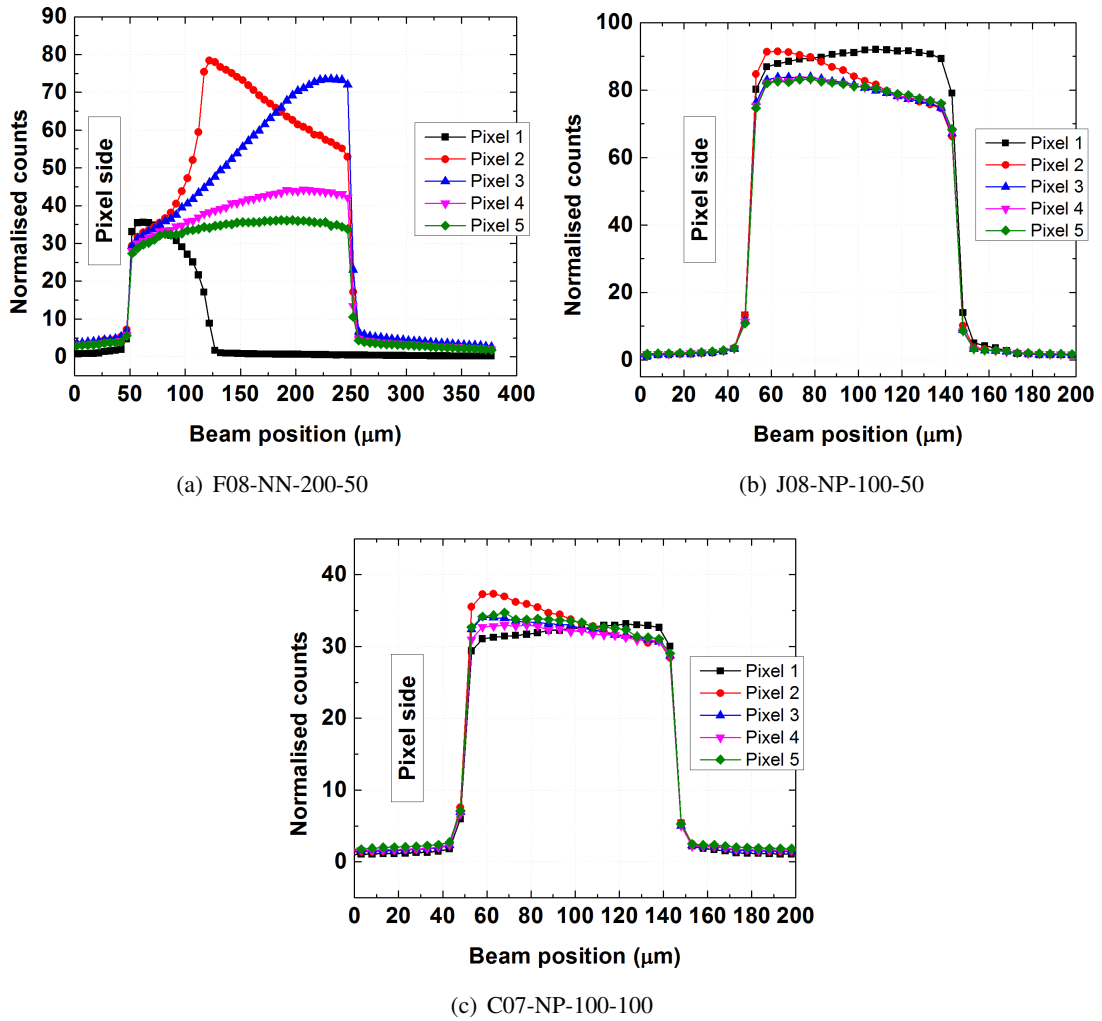
(a) F08-NN-200-50

(b) J08-NP-100-50

(c) C07-NP-100-100

Figure 7. Synchrotron side scan: pixel response as a function of incident beam position for a reverse bias of 50 V. Beam is normally incident on the side of the sensor. The counts for each pixel is normalised to the probability of 15 keV X-rays absorbed in silicon. First 5 pixels from the sensor edge are shown.

3.6 Synchrotron side scans

In this measurement the sensor face was *parallel* to incident radiation, such that the X-rays entered the sensor from the side. The beam intensity was exponentially attenuated *horizontally* across adjacent pixels of the sensor. In order to correct this effect and make the response of individual pixel comparable across the sensor, the charge in each pixel was normalised according to the probability of X-ray absorption at the pixel depth, *i.*e. the corrected number of counts collected, N', is derived from the actual number of counts collected, N, as

$$N' = \frac{N}{\Sigma_i exp(-kx_i)},$$

where x_i is the depth from the physical edge of pixel i and k is the linear attenuation coefficient for silicon for 15 keV calculated from the mass attenuation coefficient [16].

The pixel response profiles are shown in figure 7. In each plot the responses of individual pixels are overlaid. The orientation of the scan is such that the uniform implanted backside of the sensor is to the *right* of the plots and the pixellated side is to the *left*. In each case the physical dimension of the sensor's thickness is evident from the profile plot: 200 μm for F08-NN-200-50, and 100 μm for C07-NP-100-100 and J08-NP-100-50.

For F08-NN-200-50 (see figure 7(a)), the charge collection as the beam traverses the sensor's edge from pixellated to backside for the pixel closest to the physical edge is clearly non-uniform. The collected charge in all pixels (1 to 5) is approximately equal for the beam incident close to the pixellated side. As the beam travels across the sensor's edge, towards the backside implant, the collected charge in the edge pixel (pixel 1) falls to zero at a distance of 75 μm, which indicates that the field line starting from the middle of pixel 1 and 2 ends here. The charge collected in pixels 2, 3 and 4 (second, third and fourth pixel from the physical edge), however rises to be in excess of that collected by pixel 5, suggesting that a non-uniform charge collection up to pixel 4 and the fifth pixel from the edge has the uniform response expected from a standard pixel. At a beam position of approximately 75 μm from the pixel implant the charge collected by pixel 2 falls as the beam moves to the backside implant.

Over the entire sensor thickness, the charge collection in pixels 3 and 4 rises. This suggests an increasing charge collection region from the pixel side to the backside for pixels 3 and 4. Combining observations from the side and edge scans, it is concluded that charge deposited under the first pixel (edge pixel) close to the backside uniform implant is collected by the 2nd pixel.

The overall conclusion is that as the beam position moves away from the bonded edge of the outermost pixels the charge from energy deposition is carried to the neighbouring pixels where it is collected. This is consistent with observations in section 3.4, where the response of the three pixels closest to the device edge is severely distorted.

For J08-NP-100-50 (see figure 7(b)), the response of the outermost pixels is more uniform than F08-NN-200-50. However, some additional charge is induced in pixel 2 close to the collecting node. Given the shape of response of pixel 1, where around 10% more charge is collected in the region close to the pixel side compared to the back side, this indicates additional charge deflection from the outer-most pixel and implanted region. For the third pixel from the edge the charge collection is uniform and consistent with its more central neighbours (pixels 4 and 5). From this it is concluded that the sensor performs consistently starting from pixel 3.

Results for C07-NP-100-100 are similar to J08-NP-100-50. The pixel responses are shown in figure 7(c). The response of the outermost pixel is again more uniform than the F08-NN-200-50 case. Also, as in the previous case, there is consistent charge collection behaviour from the third pixel from the edge onward. The same conclusion can be drawn as for J08-NP-100-50.

In conclusion, the 200 μm thick *n-on-n* sensor has a large region at the sensor edge where the electric field is highly distorted, causing non-uniform charge collection by pixels close to the physical edge. The 100 μm thick *n-on-p* sensors are more consistent and perform almost without electric field distortion.

4 Conclusions

Three edgeless sensors fabricated utilising the active-edge technology were characterised at the B16 beamline of Diamond Light Source with monochromatic 15 *keV* X-rays and with a mini X-ray tube in the laboratory. The sensors were of *n-on-n* and *n-on-p* types with 50 and 100 μm distance between the physical edge and the first pixel, and of 100 and 200 μm sensor thicknesses. The charge collection of the sensors fabricated with the active-edge technology depends on the sensor thickness, last pixel-to-edge distance, bias voltage and probably also the sensor polarity.

The experiments demonstrated that little or no charge deposited at the edge of the sensor goes uncollected if bias voltage is not sufficient. For the *p-on-n* type sensor charge is collected in the edge pixel of X-ray incidence up to the physical end of the sensor for both devices. Charge collection is barely affected neither at normal X-ray incidence nor if illuminated from the side, due to less distorted electric field close to the sensor edge compared to the 200 μm thick *n-on-n* sensor. The counts (over-count or under-count compared to central pixels) of pixels close to the physical edge of the sensor read-out by Timepix ROICs can be corrected and calibrated.

A fabrication issue has been identified for *n-on-n* sensor in a flat-field measurement,which indicates the need for a further study needed for the process development of edgeless technology. The effect of bias voltage on charge collection at the last pixel has also been investigated. The *n-on-n* device is the most affected. The first pixel (first 55 μm) from the edge collects less charge while pixel 2 and 3 (between 55 and 165 μm from the edge) over collect compared to the other pixels. Side illumination of the device clearly indicates an insensitive region under pixel 1 where charge is deflected into neighbouring pixels.

Overall, results indicate that the active-edge technology is able to reduce the distance to the physical edge from the pixels without significant changes in charge collection rates between the pixels.

Acknowledgments

References

[1] A. Blue, M. French, P. Seller and V. O'Shea. *Edgeless sensor development for the LPD hybrid pixel detector at XFEL*, *Nucl. Instrum. Meth. A* **607** (2009) 55.

[2] G. Ruggiero, V. Eremin and E. Noschis, *Planar edgeless silicon detectors for the TOTEM experiment*, *Nucl. Instrum. Meth.* **A 582** (2007) 854.

[3] M.J. Bosma et al., *Edgeless silicon sensors for Medipix-based large-area X-ray imaging detectors*, 2011 *JINST* **6** C01035.

[4] R. Bates et al., *Characterisation of edgeless technologies for pixellated and strip silicon detectors with a micro-focused X-ray beam*, 2013 *JINST* **8** P01018.

[5] V. Fadeyev et al., *Scribe - cleave - passivate (SCP) slim edge technology for silicon sensors*, *Nucl. Instrum. Meth. A* **731** (2013) 260.

[6] J. Kalliopuska, S. Eränen, and T. Virolainen, *Alternative fabrication process for edgeless detectors on 6in. wafers*, *Nucl. Instrum. Meth. A* **633** (2011) 50.

[7] J. Kalliopuska, L. Tlustos, S. Eränen and T. Virolainen, *Characterization of edgeless pixel detectors coupled to Medipix2 readout chip*, *Nucl. Instrum. Meth. A* **648** (2011) 32.

[8] J. Kalliopuska, J. Jakubek and L. Tlustos, *Overview on Measured Properties of VTT's Edgeless Detectors and their use in High Energy Physics*, *Phys. Proc.* **37** (2012) 1046.

[9] VTT Micro and Nanoelectronics, http://www.vtt.fi.

[10] X. Wu, J. Kalliopuska, S. Eränen and T. Virolainen, *Recent advances in processing and characterization of edgeless detectors*, 2012 *JINST* **7** C02001.

[11] Diamond Light Source Ltd, http://www.diamond.ac.uk.

[12] X. Llopart, R. Ballabriga, M. Campbell, L. Tlustos and W. Wong, *Timepix, a 65k programmable pixel readout chip for arrival time, energy and/or photon counting measurements*, *Nucl. Instrum. Meth.* **A 581** (2007) 485.

[13] V. Kraus et al., *FITPix: Fast interface for Timepix pixel detectors*, 2011 *JINST* **6** C01079.

[14] T. Holy, J. Jakubek, S. Pospisil, J. Uher, D. Vavrik and Z. Vykydal, *Data acquisition and processing software package for Medipix2*, *Nucl. Instrum. Meth. A* **563** (2006) 254.

[15] J. Uher, G. Harvey and J. Jukubek, *X-ray fluorescence imaging with the Medipix2 single-photon counting detector*, *IEEE Trans. Nucl. Sci.* **59** (2010) 1067.

[16] J.H. Hubbell and S.M. Seltzer, *Tables of X-Ray Mass Attenuation Coefficients and Mass Energy-Absorption Coefficients from 1 keV to 20 MeV for Elements Z = 1 to 92 and 48 Additional Substances of Dosimetric Interest*, http://www.nist.gov/pml/data/xraycoef/ (1996).